ELSEVIER

Surface Science 493 (2001) 338–360

SURFACE SCIENCE

www.elsevier.com/locate/susc

Observation of the fcc-to-bcc Bain transformation in epitaxial Fe ultrathin films on $Cu_3Au(0\,0\,1)$

B. Roldan Cuenya, M. Doi [1], S. Löbus, R. Courths, W. Keune *

Fachbereich Physik, Gerhard-Mercator-Universität Duisburg, Lotharstr. 65, D-47048 Duisburg, Germany

Received 14 November 2000; accepted for publication 22 December 2000

Abstract

A continuous fcc-to-bcc crystallographic transition via a homogeneous tetragonal lattice deformation (Bain transformation) with increasing Fe coverage was observed in molecular-beam grown epitaxial Fe ultrathin films on $Cu_3Au(0\,0\,1)$, contrary to the usual case of a discontinuous martensitic transformation of Fe. With increasing Fe film thickness, a continuous compression of the interlayer distance perpendicular to the film plane and a simultaneous continuous expansion of the in-plane atomic distance was observed. We did not find evidence for the coexistence of fcc and bcc phases. In the ~1–12 ML (monolayer) thickness range, the films do exhibit some atomic disorder and do not grow pseudomorphous, but form twisted crystallographic domains that are rotated in the film plane about the film normal direction. The atomic volume of tetragonal states was found to follow closely face-centered tetragonal (fct) or body-centered tetragonal (bct) "epitaxial lines" according to strain-energy calculations [Surf. Rev. Lett. 1 (1994) 15], including a crossover from ferromagnetic high-moment high-volume fct to bct Fe. The results were obtained by in situ X-ray photoelectron diffraction, high-energy electron diffraction, and ^{57}Fe conversion-electron Mössbauer spectroscopy. Correlated with the Bain transformation is a Fe spin reorientation from preferentially perpendicular (for fct) to in-plane (for bct) spin direction at 25 K.

Keywords: Alloys; Single crystal surfaces; Iron; Epitaxy; Metallic films; Photoelectron diffraction; Mössbauer spectroscopy; Electron–solid diffraction; Work function measurements; Magnetic measurements

1. Introduction

Many of the unique physical and magnetic properties of bulk iron-based alloys are related to the martensitic transformation (MT), i.e. the fcc–bcc phase transformation of iron. This is a first-order *discontinuous* non-diffusive transition that involves a sudden lattice deformation via a correlated motion of groups of atoms, and large lattice strain. The MT has been investigated in bulk iron-base materials for decades [1–4]. More recently, the MT in pure ultrathin epitaxial Fe films on single-crystal $Cu(0\,0\,1)$ substrates has become the subject of considerable interest: scanning tunneling microscopy (STM) [5–8] and other techniques [9–11] including computer simulations [12] revealed a discontinuous transformation from the metastable fcc to the stable bcc phase at a critical film thickness of usually ~10 monolayers (ML) Fe upon

* Corresponding author. Tel.: +49-203-3792387; fax: +49-203-3793601.

E-mail address: keune@uni-duisburg.de (W. Keune).

[1] Present address: Department of Materials Science and Engineering, Nagoya University, Nagoya 464-01, Japan.

0039-6028/01/$ - see front matter
PII: S0039-6028(01)01239-0

increasing the thickness. In theoretical work, the energetics of the fcc–bcc MT may be described by a continuous transition known as the Bain transformation from fcc to bcc structures [13].

Already in 1924 Bain [13] suggested that an fcc phase can transform spontaneously into a bcc phase by a contraction of the interlayer spacing along the c-axis and biaxial expansion of the in-plane lattice along $\langle 1\,1\,0\rangle$ directions in the fcc(0 0 1) plane (see Fig. 1). According to Fig. 1, the lattice parameter, a_0, of the fcc lattice defines the in-plane atomic distance $a = a_0/\sqrt{2}$ and the lattice parameter $c = a_0$, being twice the interlayer distance along the c-axis.

The path of tetragonal states with $\sqrt{2} \geqslant c/a \geqslant 1$ between the fcc and bcc phases is called Bain path. It has been used to calculate the ground-state energetics of the MT [2,3,14,15]. However, one has to keep in mind that this *continuous* Bain path is a convenient theoretical tool only; to the best of our knowledge it has never been observed experimentally. Searching for a Bain transformation, pseudomorphic metal films grown on (0 0 1) surfaces of fcc substrates are attractive systems [16]. A sharp strain-driven fcc–bct phase transition of pseudomorphic Cu films on Pd(0 0 1) with increasing film thickness shows features of a Bain transition [16]. Based on a low-energy electron diffraction (LEED) and STM study, recently Lin et al. [17] suggested that the observed structural transformation from fcc(0 0 1) to bcc(0 0 1) of pseudomorphic Fe films on Cu_3Au(0 0 1) is driven by lattice-mismatch induced strain through a Bain path; however, a continuous fcc-to-bcc lattice deformation was not reported by these authors [17], and only the initial (fcc(0 0 1)-oriented) and final (bcc(0 0 1)-oriented) Fe phases of the presumed Bain transition were observed [17].

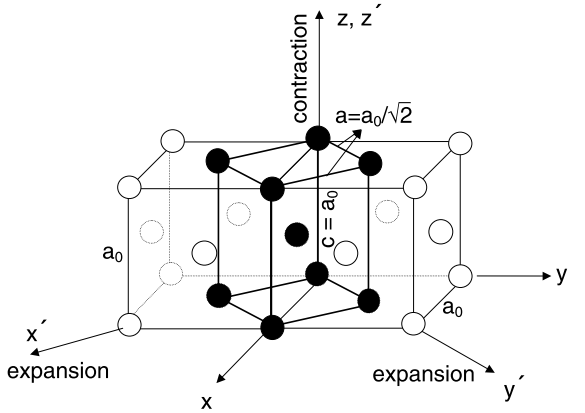

Fig. 1. Lattice distortion during the fcc–bcc transition according to Bain [13]. a_0 is the lattice parameter of the fcc unit cell.

In this work we report on the first experimental observation of the continuous fcc-to-bcc Bain transformation in ultrathin epitaxial Fe films on Cu_3Au(0 0 1) with increasing Fe coverage, contrary to the usual discontinuous MT of Fe. The out-of-plane interlayer distance ($c = a_0$, Fig. 1) and the in-plane atomic distance ($a = a_0/\sqrt{2}$, Fig. 1) of the growing Fe film were precisely determined by combining X-ray photoelectron diffraction (XPD) and reflection high-energy electron diffraction (RHEED) results. c and a values both were observed to behave monotonously as a function of film thickness from the face-centered tetragonal (fct) to the bcc region. The atomic volume of tetragonal states that are produced by epitaxial strain was found to follow closely fct or body-centered tetragonal (bct) "epitaxial lines" according to strain-energy calculations [18], with a critical value of a for crossover from the fct to the bct epitaxial line. The fct and bct states were found to be distinguishable by ^{57}Fe conversion-electron Mössbauer spectroscopy (CEMS), and a Fe spin reorientation transition was directly observed by CEMS.

The structural and magnetic properties of ultrathin epitaxial Fe films grown at room temperature or low temperature on Cu_3Au(0 0 1) have been studied in the past decade by several groups [17,19–26]. Of general interest in this system is the extreme atomic-volume dependence of ground-state magnetic properties (magnetovolume instability or low-moment/high-moment transition) predicted theoretically for bulk fcc Fe [2,27–29]. Pseudomorphic growth at RT of fcc-Fe/Cu_3Au(0 0 1) below 7 ML Fe coverage was reported by Lu et al. [19], Rochow et al. [21], and Baudelet et al. [23], based on LEED results. Considering the relatively large lattice misfit (4.2%) of bulk fcc (γ)-Fe ($a_0 =$ 3.59 Å at 293 K) and Cu_3Au ($a_0 = 3.75$ Å), a tetragonal distortion (fct structure) in the Fe films

was not excluded in Ref. [23]. Upon increasing the Fe coverage, Lin et al. [17,24] reported an fcc-to-bcc transformation at a critical thickness of 3.5 ML for RT growth, correlated with a magnetization reorientation transition from perpendicular to in-plane direction, (observed earlier in Ref. [23]), and the coexistence of fcc-like and bcc-like phases from 3.5 ML up to ~6 ML Fe. By contrast, Schirmer et al. [26] conclude from quantitative LEED results that 3.3–4.8 ML thick films are strained bcc Fe(0 0 1) rather than the previously proposed fcc structure.

In our photoelectron study of Fe/Cu_3Au(0 0 1) we used photoelectron diffraction of core electrons (XPD) and angle-resolved photoelectron spectroscopy (ARXPS and ARUPS along the surface normal). We focussed our attention to the application of the forward scattering (FS) enhancement in XPD for a quantitative investigation of growth and structure of Fe/Cu_3Au(0 0 1). XPD can provide accurate information on the local structure of the near-surface region [30,31]. Since the scattering of medium-energy electrons (above several hundred eV kinetic energy) by lattice atoms is predominantly in the forward direction, the photoelectron intensity is enhanced in the direction connecting the emitter atom with the overlying scatterer atoms. The interpretation of intensity angular distributions (IADs) is thus straightforward for low-indexed crystallographic directions and yields atom-specific local structure informations. Thus, XPD has been used recently to determine the growth and structure of epitaxial ultrathin metal films [32,33]. XPD is particularly well suited for structural studies of ultrathin films, because the core-level photoelectron FS is a short-range order effect, and in addition, due to the kinetic energy of the photoelectron which identifies it as originating from a specific core level, film and substrate scattering can be easily distinguished. ARUPS was used to measure the work function development with increasing Fe film thickness.

2. Experimental

Our samples were prepared under similar conditions by molecular beam epitaxy in two separate ultrahigh vacuum (UHV) chambers, one system for RHEED/LEED, Auger electron spectroscopy (AES) and in situ CEMS studies, and the other one for photoelectron spectroscopy and LEED investigations.

The RHEED/LEED and CEMS experiments were performed in the first UHV system with a base pressure $\leqslant 6 \times 10^{-11}$ mbar. The pressure during film deposition never exceeded 2×10^{-10} mbar. A disk-shaped Cu_3Au(0 0 1) single crystal with the (0 0 1) plane oriented to within 0.5° was used as substrate. The mechanically polished substrate surface was initially treated by Ar^+ ion sputter cleaning at 473 K (2–3 h at 1 keV) until no impurities could be detected by AES. Subsequent Ar^+ sputter smoothing of the surface (at 0.5 keV) was achieved at 473 K for 40 min. The atomically ordered Cu_3Au(0 0 1) surface was obtained after subsequent annealing at 720 K for 1 h, at 690 K for 1 h, and finally at 600 K for 15 h [34], i.e. below the chemical order–disorder transition temperature of 663 K for Cu_3Au. Several cycles of sputter smoothing and annealing were performed, until sharp half-integer streaks of the c(2 × 2) superstructure appeared in the RHEED pattern (Figs. 2(a), (e), and Fig. 3), in addition to the fundamental streaks, revealing the well ordered atomically flat Cu_3Au(0 0 1) surface. RHEED was used to select the azimuthal orientation of the Cu_3Au-(0 0 1) surface with an accuracy of ±1°. The iron films were deposited from shielded water-cooled Knudsen cells with alumina crucibles. Natural Fe (99.9985 at.% purity) or ^{57}Fe metal (95.5% isotopic enrichment) were used as starting materials. The evaporation sources were outgassed and stabilized carefully prior to sample deposition. The film thickness and deposition rate (1.8 Å/min) were measured by quartz-crystal microbalances that were calibrated previously by RHEED intensity oscillations observed during fcc-Fe deposition onto a clean Cu(0 0 1) substrate. The film thicknesses are estimated to be accurate within ±10%. During deposition, the substrate temperature, though nominally RT, increased continuously up to ~40°C for the thickest films, as measured by the thermocouple of the sample holder. RHEED patterns were recorded during growth by a CCD camera connected to a computerized data storage and

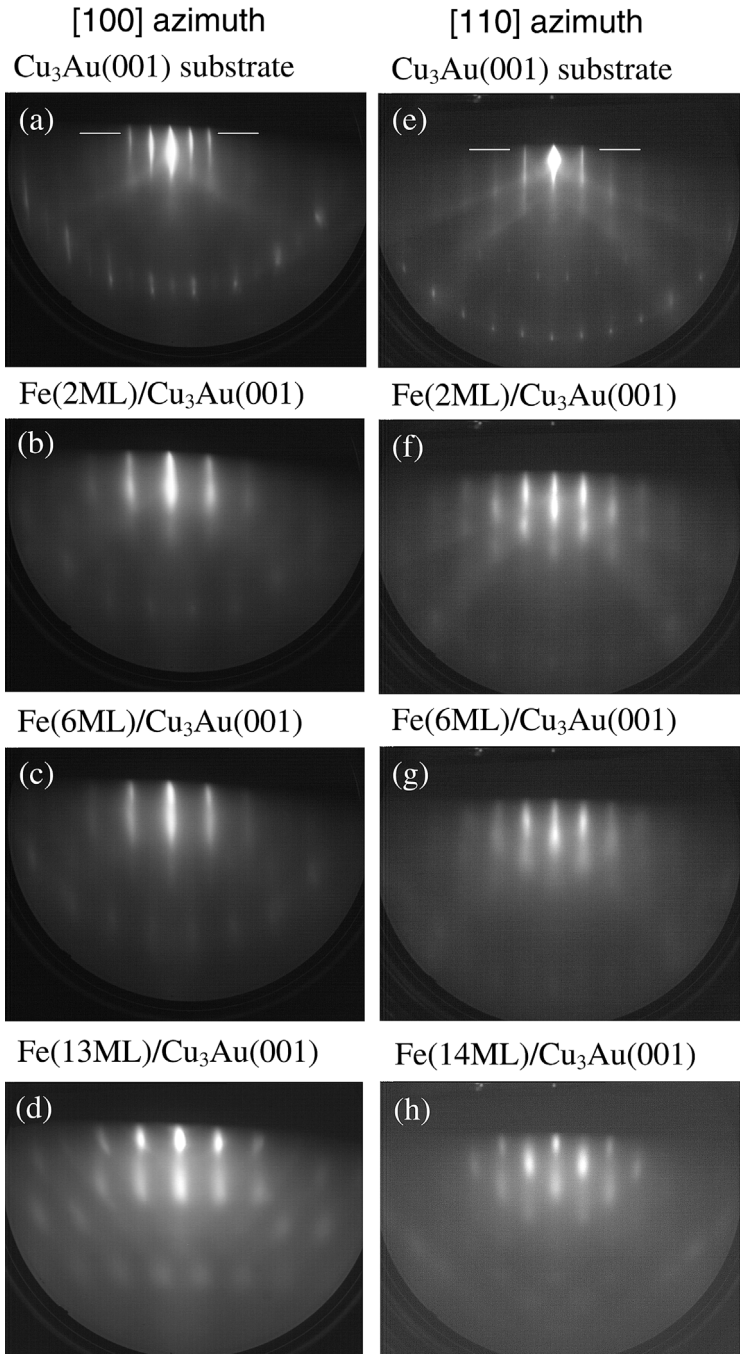

Fig. 2. RHEED patterns along the $[1\,0\,0]_{fcc}$ azimuth (left) and $[1\,1\,0]_{fcc}$ azimuth (right) of $Cu_3Au(0\,0\,1)$: clean atomically ordered (2×2) $Cu_3Au(0\,0\,1)$ surface (a) and (e), covered by 2 ML Fe (b) and (f), 6 ML Fe (c) and (g), and 13 ML Fe (d) and 14 ML Fe (h). Beam voltage: 12 kV, angle of incidence $\sim 3°$.

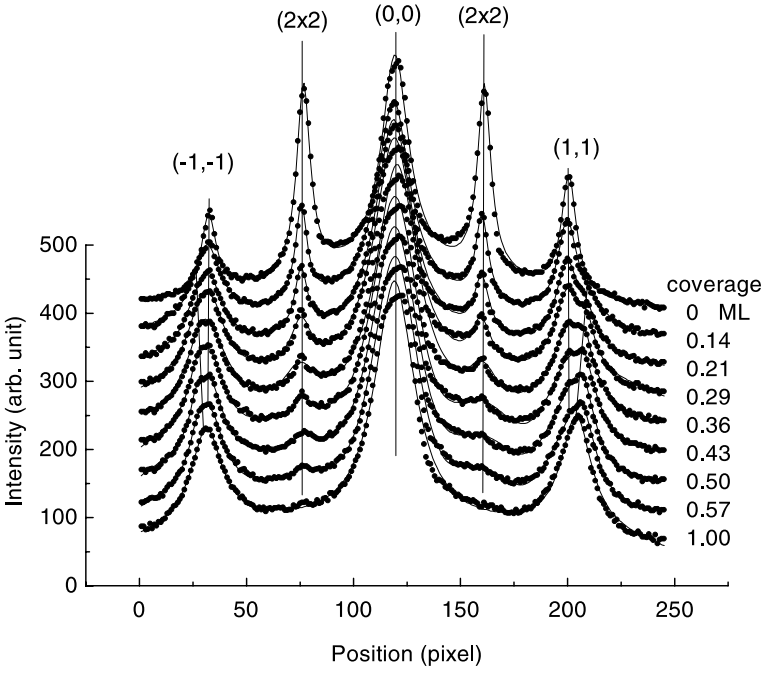

Fig. 3. Typical RHEED intensity profiles along the horizontal direction marked by a white line in Fig. 2 (a), as a function of Fe film thickness in the low-coverage regime. The (2 × 2) superstructure peaks and the fundamental (1,1) and (−1,−1) peaks of clean Cu_3Au (top) disappear near ~1.0 ML Fe (vertical lines). The separation of the (1,1) and (−1,−1) peaks of Fe (evidenced as shoulders for small coverages) is clearly larger than that of Cu_3Au in this coverage regime, but decreases with increasing coverage (tilted straight lines). Data points were least-squares fit with Lorentzian lines and a (weak) smooth background intensity. The fit curves are indicated by solid lines.

processing system. ^{57}Fe CEMS spectra were measured in situ in UHV, with the sample transferred to the UHV cold finger of a liquid He-cooled flow cryostat. Electrons emitted from the sample surface after the nuclear resonant absorption were detected by a channeltron [35]. A ^{57}Co-in-Rh Mössbauer source of ~100 mCi activity was used. The incoming 14.4 keV γ-ray entered the UHV chamber through a Be window in normal incidence to the film plane.

Photoelectron spectroscopy and LEED experiments were performed in a second UHV system with a base pressure of 5×10^{-11} Torr or better. The system comprises two subchambers for substrate preparation and thin-film epitaxy, ARXPS and visual LEED. Photoelectrons were excited with unmonochromatized MgKα radiation ($h\nu = 1486.6$ eV). ARXPS spectra (energy distribution curves) were taken along the surface normal and polar-scanned angular distributions of substrate and adsorbate core-level intensities (XPD polar scans) were measured in the symmetry planes along the two principal azimuths, [1 0 0] and [1 1 0], in the Cu_3Au(0 0 1) surface plane. A VG ESCALAB MARK II spectrometer with a fixed angle between the incident photons and the electron collection direction (38°), an angular resolution of about 5° and an overall energy resolution of about 0.8 eV was used. The sample manipulator was rotated to scan the electron detection polar angle and the XPD data were gathered in running the peak emission intensities with fixed analyzer energy (fixed binding energy) and angular steps of 1°. All experiments have been carried out with a disk-shaped Cu_3Au(0 0 1) single crystal with the (0 0 1) plane oriented to within 0.5° and which was prepared as described in Refs. [36–38]. It was cleaned in situ by cycles of Ar ion-bombardment (500 eV

beam energy) and subsequent annealing up to 640 K (below the phase transition temperature of 663 K) until sharp LEED patterns (a Cu(0 0 1)-(2×2) structure) indicated a well-ordered surface at room temperature. The temperature was controlled by a thermocouple. The surface cleanliness was checked by XPS and XAES. With ARUPS we looked for the existence of valence-band surface states [36,37] which were used as a further reference for the quality of surface. LEED was used to perform the azimuthal orientation of the surface with an accuracy of $\pm 1°$. The iron films were deposited from a shielded, water-cooled metal source through vapor deposition using a Fe wire of 99.999% purity. The source was outgassed and stabilized very carefully prior to each deposition. During Fe deposition, the pressure of the chamber increased to about 5×10^{-10} Torr. The deposition rate was fixed at 0.5 Å/min by controlling the temperature of the source with the use of a quartz microbalance signal. The quartz monitor could not be brought exactly at the sample position, thus film thicknesses were determined with the use of the Cu3p and Au4f core-level photoemission intensities of the substrate (to be reported below). The film thicknesses are quoted below in monolayers (ML) and the absolute coverages given in this paper were estimated to be accurate to within $\pm 10\%$ (to be discussed below). All preparation and photoemission experiments were performed with the substrate nominally at RT. During Fe deposition, the temperature of the sample increased with a rate of about 0.6°C/Å up to 330 K after completion of the thickest film (34 Å).

3. Results and Discussion

3.1. RHEED: in-plane atomic spacing

Typical RHEED patterns at various Fe coverages are shown in Fig. 2 for the $[1\,0\,0]_{fcc}$ azimuthal direction (Fig. 2(a)–(d)) and $[1\,1\,0]_{fcc}$ azimuthal direction (Fig. 2(e)–(h)) of $Cu_3Au(0\,0\,1)$. (These directions are also labeled [1 0 0]CA and [1 1 0]CA, respectively, in our work.) The half-integer (2×2) superstructure streaks of the ordered flat Cu_3Au-(0 0 1) surface (Fig. 2(a)) were found to persist for small coverage ($\lesssim 1$ ML), but disappear at larger Fe thicknesses, where only fundamental streaks are observed, as can be seen for 2 and 6 ML in Fig. 2(b), (f) and Fig. 2(c), (g), respectively. Fig. 2 demonstrates that the Fe films up to 6 ML thickness grow epitaxially, presumably with fcc-like structure, and a rather flat surface. Compared with the pattern of the clean substrate, the streaks of the Fe films are broadened, indicating some structural disorder or atomic-scale surface roughness. At 13–14 ML coverage the RHEED pattern changes to a dot-type pattern that is typically observed in 3-dimensional (3D) film growth; this pattern indicates 3D growth of epitaxial (presumably bcc-like) Fe.

The separation of the RHEED streaks in reciprocal space is a measure for the in-plane atomic spacing in real space [39] in a direction perpendicular to the scattering plane. The in-plane atomic spacing of the growing Fe film relative to that of the substrate was determined from the measured distance in reciprocal space between (−1,−1) and (1,1) streaks observed along the $[1\,0\,0]_{fcc}$ azimuth of $Cu_3Au(0\,0\,1)$, and between (−1,0) and (1,0) reflections observed along $[1\,1\,0]_{fcc}$ of $Cu_3Au(0\,0\,1)$. RHEED intensity profiles were measured along the horizontal direction marked by the white lines in Fig. 2(a), (e), for various Fe coverages. Typical intensity profiles for the $[1\,0\,0]_{fcc}$ azimuth are shown in Fig. 3. The (2×2) superstructure peaks of the substrate are observed up to ~1 ML coverage, indicating Fe island growth in this thickness regime, in agreement with STM results of Ref. [17]. By least-squares fitting the measured intensity profiles with Lorentzian lines (as described in Fig. 3) the peak positions of the RHEED reflections (and consequently the in-plane atomic spacing) can be obtained with high precision [39,40]. The separation of the fundamental peaks of Fe (seen as outer shoulders in the (−1,−1) and (1,1) peaks for small coverages) clearly decreases continuously with increasing Fe film thickness (Fig. 3), implying a continuous increase of the atomic distance perpendicular to the scattering plane.

The apparent in-plane atomic distance a (relative to that of the substrate) of the planar Fe unit cell as a function of Fe coverage, as deduced from the apparent separation of the fundamental peak

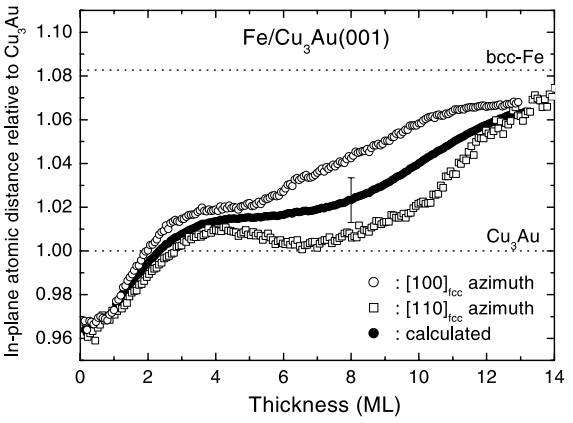

Fig. 4. Fe thickness dependence of the in-plane atomic nearest-neighbor distance, a, relative to that of Cu_3Au, as obtained from the RHEED streak separation along $[1\,0\,0]_{fcc}$ (○) and $[1\,1\,0]_{fcc}$ (□) azimuthal directions. Closed circles: calculated values as described in the text and Fig. 5.

positions in reciprocal space, is shown in Fig. 4 for the $[1\,0\,0]_{fcc}$ azimuth (open circles) and for the $[1\,1\,0]_{fcc}$ azimuth (open squares). It is unexpected that these apparent relative a values do not coincide for both azimuthal directions in the coverage regime between ~1 and 13 ML, but show very different behavior. This demonstrates that the concept of a perfect Fe lattice in complete registry with the underlying substrate lattice (i.e. pseudomorphic growth) must be abandoned. Instead, we have to assume that the Fe films show some degree of atomic disorder and grow in crystallographic domains that are not exactly in registry with the fcc substrate. In order to deduce the true in-plane atomic spacing of the Fe films we have adopted the structural model sketched in Fig. 5(a), which is based on three assumptions: (i) the planar unit mesh remains a square, (ii) the Fe films grow in form of crystallographic "twist" domains, and (iii) a certain intrinsic atomic disorder exists in the Fe lattice that leads to a specific lateral broadening of the reciprocal lattice rods. The model is outlined in more details as follows.

Fig. 5(a) shows a schematic view of the Fe reciprocal lattice along the surface normal direction (view onto the surface plane). The original square reciprocal lattice of ordered Fe, that is in registry with the underlying $Cu_3Au(0\,0\,1)$-substrate lattice, is indicated by small black dots (projection of reciprocal lattice rods) forming the full-drawn square. The original separation of the (−1,0) and (1,0) reflections, as observed from the $[1\,1\,0]_{fcc}$ azimuthal direction, is indicated by heavily dotted horizontal arrows (labeled "original"). Similarly, the original separation of the (−1,−1) and (1,1) reflections, as observed from the $[1\,0\,0]_{fcc}$ azimuth, is indicated by heavily dotted diagonal arrows (also labeled "original"). Two "twisted" square reciprocal lattices which arise by simple symmetrical rotation of the original reciprocal lattice by a positive and negative "twist angle", respectively, are indicated by the two lightly dotted squares. The reciprocal lattice rods of the twisted lattices are assumed to be laterally elongated in the rotational direction, as shown schematically by the ellipsoidal streaks in Fig. 5. We speculate that such a special streak shape might be caused by some type of crystallographic disorder, possibly induced by twist and/or tilt boundaries due to a large density of screw dislocations [41]. In STM observations on $Fe/Cu_3Au(0\,0\,1)$ by Lin et al. [17] a network-like surface topography with a lateral period of 3–5 atoms was possibly connected with screw dislocations. The presence of atomic disorder is also evident from the relatively large linewidths observed in the Mössbauer spectra (see Section 3.3 below). It is shown by XPD in Section 3.2.4 (below) that the behavior of the Fe3p forward scattering intensity as a function of Fe film thickness is compatible with the atomic disorder/twisted domain model.

The intersections of these reciprocal lattice rods of elongated cross-section (Fig. 5(a)) with the Ewald sphere then result in a slightly *larger* separation (as compared with that of the original reciprocal lattice) between the (−1,0) and (1,0) reflections (indicated by the horizontal black arrows marked "twist"), when observed along the $[1\,1\,0]_{fcc}$ azimuth. The reverse is the case for the $[1\,0\,0]_{fcc}$ azimuthal direction: here, the apparent separation between the (−1,−1) and (1,1) reflections (indicated by the diagonal black arrows marked "twist") is slightly *smaller* than the corresponding separation in the original reciprocal lattice. Since the spot separation in reciprocal space is inversely proportional to the periodicity in the

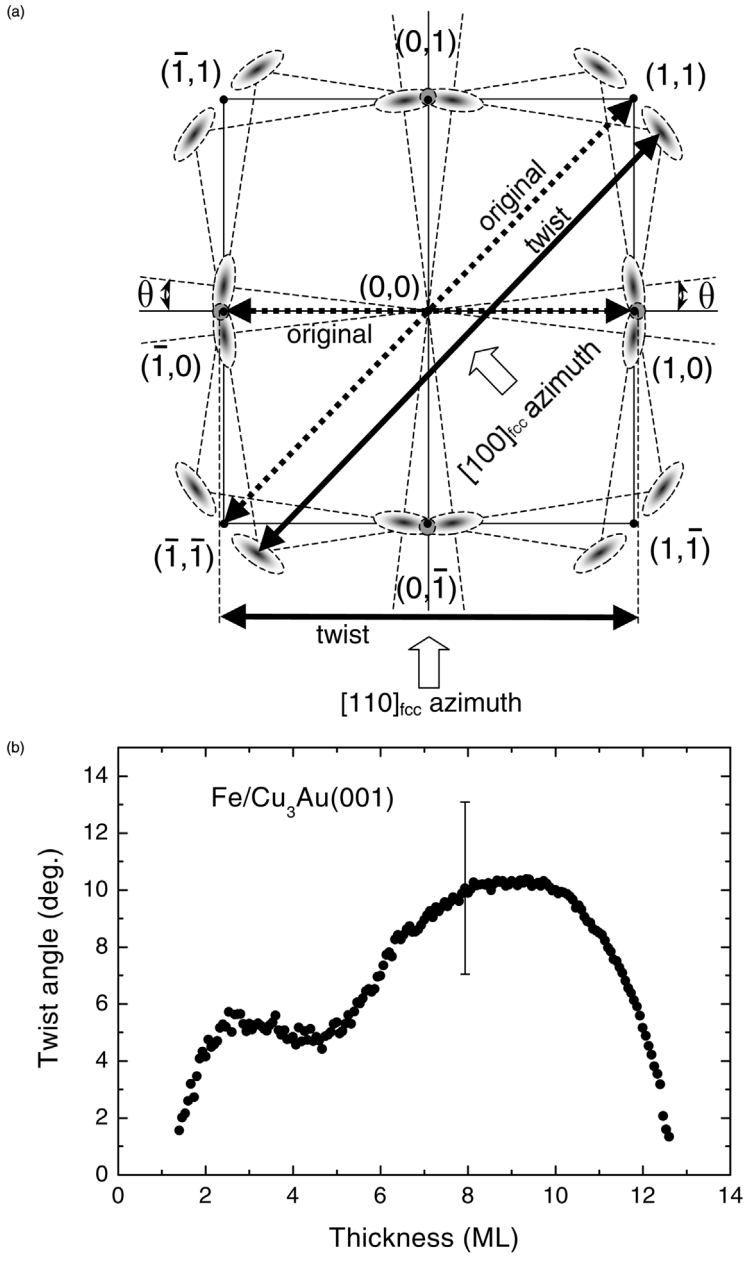

Fig. 5. (a) View along the surface normal direction (onto the surface plane) of the reciprocal lattice of the Fe film (schematic drawing). The original (square) reciprocal lattice is indicated by small black dots (reciprocal lattice rods) forming the full drawn square. Two twisted square reciprocal lattices which are rotated symmetrically relative to the original reciprocal lattice by a positive or negative twist angle, respectively, are indicated by the two lightly dotted squares. The lattice rods of the twisted reciprocal lattices are assumed to be laterally elongated, as indicated schematically by ellipsoidal streaks. When viewed along $[1\,1\,0]_{fcc}$ or $[1\,0\,0]_{fcc}$ azimuthal directions, the intersections of these elongated rods with the Ewald sphere then lead to slightly different separations of reflections (as indicated by the horizontal and diagonal black arrows labeled "twist") when compared with the corresponding separations in the original reciprocal lattice, (for further details, see text). (b) Twist angle versus Fe film thickness resulting from the model in (a) and from the measured data in Fig. 4, leading to the calculated in-plane atomic distance in Fig. 4.

real lattice, then our model explains the different behavior (Fig. 4) of the apparent in-plane atomic separations measured along the $[1\,1\,0]_{fcc}$ and $[1\,0\,0]_{fcc}$ azimuthal directions: the apparent in-plane atomic distance determined along the $[1\,0\,0]_{fcc}$ azimuth is larger than that measured along the $[1\,1\,0]_{fcc}$ azimuth. This difference appears in that Fe thickness region where the assumed twisted crystallographic domains are present.

We have calculated the "true" in-plane lattice parameter within a twisted domain of the Fe film from the measured data in Fig. 4 along the $[1\,0\,0]_{fcc}$ and $[1\,1\,0]_{fcc}$ azimuths by applying the described model and assuming the "best" twist angle that yields self-consistency. The Fe thickness dependence of the calculated true in-plane atomic spacing, a, and of the corresponding twist angle are shown in Fig. 4 (closed circles) and Fig. 5(b), respectively. Fig. 5(b) shows that the twist angle first increases with increasing Fe coverage from near 0° up to about $10 \pm 3°$ at 8–10 ML Fe, and then decreases to zero again. The deduced in-plane atomic distance, a, of Fe (Fig. 4, closed circles) exhibits monotonical behavior as a function of Fe coverage. Below ~2 ML Fe, a values are observed to be smaller than that of the $Cu_3Au(0\,0\,1)$ substrate ($a_0/\sqrt{2} = 2.652$ Å for Cu_3Au), possibly due to a surface contraction during island growth, similar to the fcc-Co/Cu(0 0 1) and fcc-Fe/Cu(0 0 1) systems [39,40]. Between ~3.5 and 6.5 ML Fe, the in-plane atomic distance exhibits a plateau-like behavior near 2.685 ± 0.006 Å, which is slightly larger than that of the substrate (2.652 Å), but is considerably smaller than the in-plane atomic distance (lattice parameter) of bcc-Fe(0 0 1) ($a_0 = 2.866$ Å). This is a hint to Fe growth with distorted fcc structure in this coverage regime. For 13.5 ML Fe we determined an in-plane atomic distance of 2.819 ± 0.013 Å, which is closer to the lattice parameter of bcc Fe ($a_0 = 2.866$ Å), indicating a transition to distorted bcc Fe.

We have also measured the specular RHEED intensity along $[1\,0\,0]_{fcc}$ and $[1\,1\,0]_{fcc}$ azimuths during deposition as a function of Fe thickness. The result (not shown) is similar to the specular MEED-intensity behavior in Ref. [17], that is characterized by several regions of growth: region A (for island growth between 0 and 2.5 ML), region B (for layer-by-layer-like growth with large average roughness between 2.5 and 5.5 ML, including three RHEED oscillations with 1 ML period), and region C (for film morphology with large roughness above 6 ML, characterized by a continuous RHEED intensity change).

3.2. ARXPS and XPD: out-of-plane interlayer spacing

3.2.1. Calibration of the Fe film thicknesses (ARXPS)

Normal emission XP spectra containing the Fe3p and Fe3s core-levels of the Fe film as well as the Au4f and Cu3p levels of the substrate were measured as a function of the Fe film thickness (Fig. 6; see also Fig. 2 of Ref. [32]). With increasing film thickness, the Fe signals increased and the substrate signals decreased monotonically, until above about 30 ML the Cu 3p signal was no longer visible above the background of inelastically scattered electrons. However, as can be seen from Fig. 6, a weak Au4f signal was still detectable at these coverages, indicating that some Au atoms diffuse to the surface region of the Fe film (to be discussed below).

For the determination of the film thickness, the Cu3p normal emission intensities were used. The procedure has been described in detail for Fe/Au(0 0 1) in Ref. [32] and therefore we only summarize the most important points. (i) A Tougaard-like inelastic background was first subtracted from the original spectra yielding the elastic spectra. (ii) We emphasize that in the low-coverage region of up to about 8 ML the elastic intensities do not follow a simple exponential decay with increasing Fe film thickness. This is due to the strong attenuation of the forward scattering by multiscattering with increasing number of scattering atoms above the emitter atom. (iii) An exponential decay of the elastic intensities is however observed above 8 ML, where diffraction effects on the substrate emission by the overlaying Fe film are washed out effectively. In this thickness region of isotropic substrate emission the substrate intensity (index S) is given by

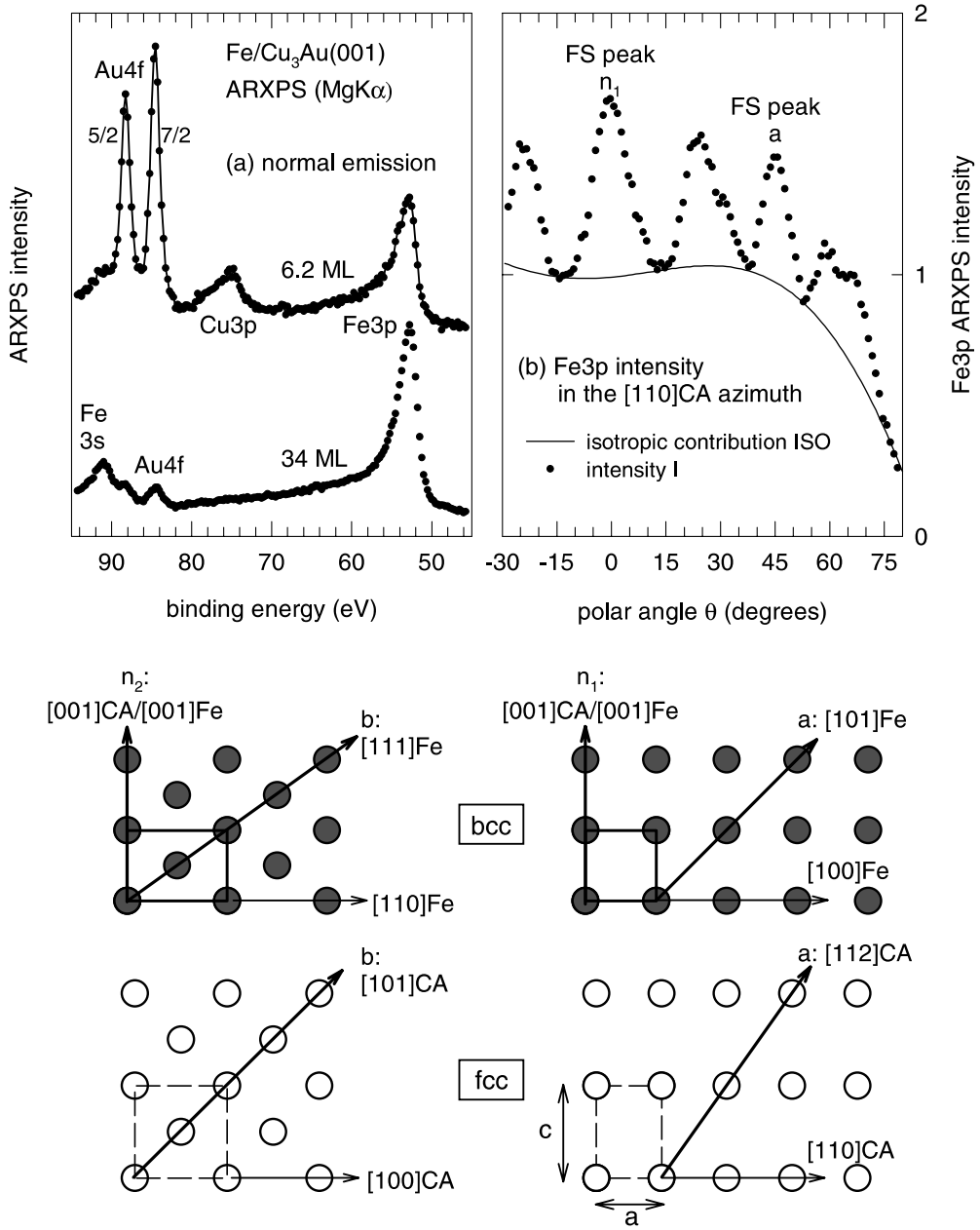

Fig. 6. Left panel above: ARXPS spectra from 6.2 and 34 ML Fe on $Cu_3Au(0\,0\,1)$ taken along the surface normal using MgKα radiation. The spectra comprise the emissions from the upper substrate and film core states, Au4f and Cu3p and Fe3s and 3p, respectively. A Tougaard-like inelastic background has already been subtracted from the spectra. Right panel above: Fe3p polar-scanned IAD (Fe3p XPD) for a 31.7 ML thick Fe film taken in the $[1\,1\,0]_{fcc}$ azimuth of the substrate (labeled [1 1 0]CA). The data have been corrected for background. The solid line represents the isotropic contribution, ISO, to the Fe3p IAD. The intensity I is normalized to $ISO(0°) = 1 - \exp(-31.7/L\ (\text{in ML})) \cong 1$ where L is the EAL, for details see text. Below: Side views of the geometric structures of ideal bcc-Fe(0 0 1) and ideal fcc-Fe(0 0 1) on fcc-$Cu_3Au(0\,0\,1)$ along the [1 1 0] and [1 0 0] azimuthal directions of the substrate (CA). The directions for next-neighbour FS (a and b) and FS along the surface normal (n_1 and n_2) are indicated by the arrows and their crystal indices. The lattice parameters c and a are indicated.

$$I_S \text{ (diffraction free)} \equiv \mathrm{ISO_S}(t) = \mathrm{ISO_S}(0)\exp(-t/L_{Fe}), \quad (1)$$

where $\mathrm{ISO_S}(0)$ is the substrate signal at zero coverage and L_{Fe} is the effective attenuation length (EAL) of the photoelectrons in the Fe film with thickness t. It has been shown in Ref. [32] that the EAL as given by Seah and Dench [42] is a very good approximation. Our Cu3p data fit rather well to such an exponential for $t > 7$ ML. The quartz monitor has been calibrated applying Eq. (1) using an EAL of 12.6 Å: The conversion from Å to ML was done using an perpendicular interlayer distance $c/2 = a_0(\text{bcc-Fe})/2 = 1.433$ Å above 7 ML. Below 7 ML the variation of c/a (see below) has been taken into account. We believe that the accuracy of our thickness scale is about 10%. It should also be mentioned that Eq. (1) is only valid for an ideal layer-by-layer growth (Franck–van der Merwe (FM) growth mode). (iv) In the diffraction region below 7–8 ML, the angle dependent AR-XPS intensity from the substrate, $I_S(t)$, can be described as a sum of isotropic emission $\mathrm{ISO_S}(t)$ and an additional term due to FS and diffraction, which we call the anisotropic emission $A_S(t)$:

$$I_S(t;\theta) = \mathrm{ISO_S}(t;\theta) + A_S(t;\theta), \quad (2)$$

where θ is the polar emission angle along a certain azimuth in the substrate surface with respect to the surface normal. If one assumes that A is zero for four scatterers [32], the vanishing of A in our experiments at 7 ML Fe indicates a top layer of Au atoms on the Fe film (see below) in agreement with the residual Au4f signal at high coverages.

3.2.2. Fe3p ARXPS and XPD

As for the substrate, an isotropic (ISO) and an anisotropic (A) term contribute to the elastic core-level ARXPS intensities of the Fe film, both depending on thickness t and polar angle θ [32]:

$$I(t;\theta) = \mathrm{ISO}(t;\theta) + A(t;\theta). \quad (3)$$

For the film photoelectrons, both ISO and A increase with t. For normal emission ISO is given by an exponential increase as:

$$\mathrm{ISO}(t;0^\circ) = \mathrm{ISO}_\infty(0^\circ)[1 - \exp(-t/L_{Fe})], \quad (4)$$

where $\mathrm{ISO}_\infty(0^\circ)$ is the isotropic adsorbate signal for an infinitely thick layer and L is the EAL as derived from the decay of the substrate signal (see above). In agreement with Eq. (3) and with our study of Fe/Au(0 0 1) [32] the Fe3p intensities as extracted from the normal emission XP spectra (left upper panel of Fig. 6), $I_{XPS}(t;0^\circ)$, do not at all fit to a simple exponential increase with t, evidencing the existence of a contribution A along the surface normal with a nonexponential increase with t.

The anisotropic term A also increases with the number of scatterers above the emitter along the line of detection, but already saturates for about four scatterers [32]. The Fe3p polar scan (PS; also called XPD diagram in the following) presented for a 31.7 ML thick Fe film as an example in the right upper panel of Fig. 6 reveals the angular dependence of A for a well-ordered Fe film with bcc(0 0 1) structure (to be discussed below). We mention here that all XPD diagrams shown in this paper have been corrected for background (for details see Ref. [32]). The isotropic emission is indicated by the solid line, which has been obtained by a polynomial fit (of fifth degree) to the minima in the angular distribution. This choice of ISO (the shape of which is very much influenced by the experimental apparatus) is of course an approximation, which however can be justified as follows. The Fe3p polar scan anisotropy at zero polar angle, $A_{PS}(0^\circ) := I_{PS}(0^\circ) - \mathrm{ISO}(0^\circ)$, of a thick film (34 ML) amounts 0.65 relative to $\mathrm{ISO}(\infty;0^\circ) = 1$. Using this value to scale the measured XPS intensities $I_{XPS}(t;0^\circ)$, we found that the difference $A_{XPS} := I_{XPS}(t,0^\circ) - \mathrm{ISO}_{XPS}(t;0^\circ)$ (ISO from Eq. (4)) is in good agreement with $A_{PS}(0^\circ)$ for the whole thickness range investigated, showing that the used definition of ISO in the polar scans is a good one.

Fe3p polar scan IADs have been measured along the two principal azimuths of $Cu_3Au(0\,0\,1)$ (we use the abbreviation CA for the substrate in the following), $x = [1\,0\,0]\text{CA}$ and $\bar{x} = [1\,1\,0]\text{CA}$ (see Fig. 6). Fig. 7 shows the corresponding relative anisotropies of the IADs defined in this paper as:

$$\mathrm{ANISO}(\theta) = (I_{PS}(\theta) - \mathrm{ISO}(\theta))/\mathrm{ISO}(\theta) = A(\theta)/\mathrm{ISO}(\theta). \quad (5)$$

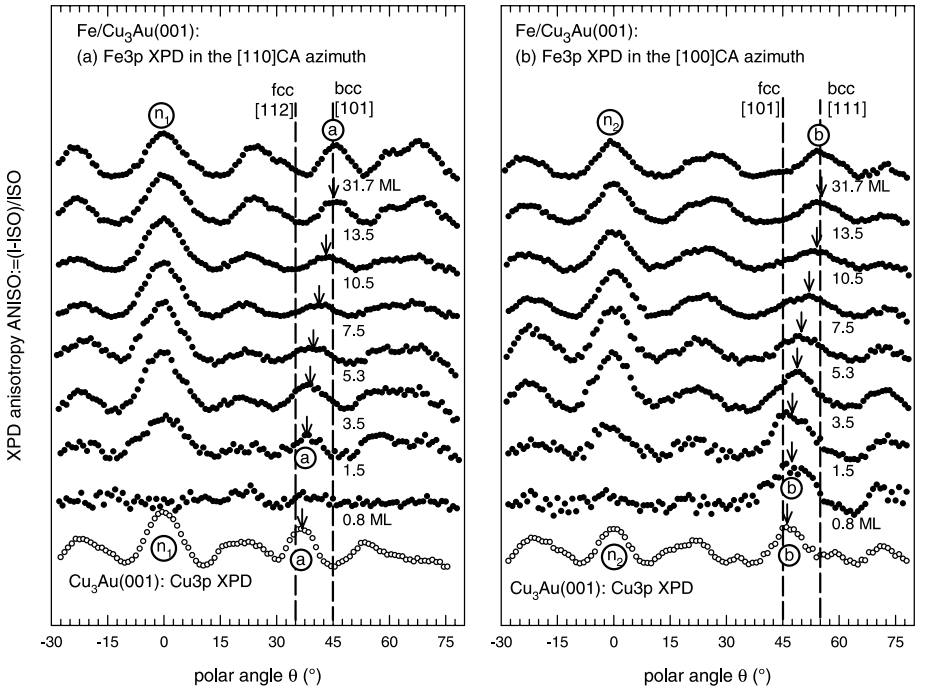

Fig. 7. Polar anisotropies ANISO := $(I - \mathrm{ISO})/\mathrm{ISO}$ of the Fe3p IADs (Fe3p XPD) with increasing Fe coverage on $Cu_3Au(0\,0\,1)$ from 0.8 ML (bottom) to 31.7 ML (top). Left: [1 1 0]CA azimuth. The vertical dashed lines indicate the polar angles of fcc-[1 1 2] and bcc-[1 0 1] directions, respectively. Right: [1 0 0]CA azimuth. The vertical dashed lines indicate the polar angles of fcc-[1 0 1] and bcc-[1 1 1] directions, respectively. In both panels, the arrows indicate the continous shift of the forward scattering peaks a and b (compare with Fig. 6).

Up to about $\theta = 60°$, the difference between A and ANISO is so small that it cannot recognized. (Note that in Ref. [32] we used the somewhat different definition $A_{\mathrm{XPD}}(\theta) = [I_{\max}(\theta) - I_{\min}(0°)]/I_{\min}(0°)$ with the identification $I_{\min}(\theta = 0°) = \mathrm{ISO}(\theta = 0°)$). $\mathrm{ISO}(\theta)$ is normalized at zero polar angle according to Eq. (4). For comparison the corresponding Cu3p anisotropies of the clean substrate are also shown in this figure.

Besides the normal emission FS maxima (designated with n), the Fe3p anisotropies exhibit pronounced next-neighbour FS peaks in the polar angle regions indicated by dashed lines: peak a between 35° and 45° along [1 1 0]CA and peak b between 45° and 55° along [1 0 0]CA, respectively. The origin of a and b is indicated in Fig. 6 for fcc and bcc structures, respectively. The variation of the polar angle and the strength of a and b with increasing film thickness will be discussed in detail below. The other peaks on both sides of a and b are due to scattering by more distant atoms (see Fig. 6) and second-order diffraction. They show a somewhat more complex structure due to interference effects and only serve as structural fingerprints in this paper.

Above about 13.5 ML the FS peaks a and b appear at 45° along [1 1 0]CA and 55° along [1 0 0]-CA, respectively. These polar angles are characteristic for the next neighbour [1 0 1] and [1 1 1] directions, respectively, of a bcc(0 0 1) unit cell rotated by 45° about the surface normal (see. Fig. 6). Indeed the identity (within the scatter of the data) of the Fe3p XPD diagrams of "thick" films on $Cu_3Au(0\,0\,1)$ and on $Au(0\,0\,1)$, where the bcc-(0 0 1)-R45° structure of the Fe film is well established [32], does not allow any doubt about the bcc(0 0 1) structure of Fe films on $Cu_3Au(0\,0\,1)$ above about 13.5 ML.

3.2.3. c/a ratio as function of film thickness

In order to determine the development of the c/a ratio with increasing Fe thickness the FS features a and b are relevant in this context. At very low coverages peak a along [1 1 0]CA appears at $\theta = 38°$ being only slightly larger than 35.2°, which is the ideal FS angle along the [1 1 2] atomic rows of fcc-Fe(0 0 1) (left dashed vertical line in the left panel of Fig. 7). Accordingly peak b along [1 0 0]-CA appears at about the corresponding [1 0 1] atomic rows at 45° (left dashed line in the right panel of Fig. 7). Thus, at very low coverages the Fe film grows with an fcc(0 0 1)-like structure.

With increasing Fe coverage both these FS features shift continuously (indicated by the arrows in Fig. 7) towards the larger polar angles of the next-neighbour directions of the bcc(0 0 1)-R45° structure discussed above. This indicates that the fcc-like film is progressively strained along the normal direction by a compression of the interlayer distance c (to be discussed below together with the results from RHEED for the in-plane atomic distance a).

The c/a ratio of the growing Fe film is simply obtained using the relation (obvious from Fig. 6) $c/a = \tan\theta_{FS}$, where θ_{FS} is the polar angle for the FS features a and b, respectively. The results for the two azimuths investigated are given in the upper panel of Fig. 8. Both data sets agree within the error bars. The open diamonds in the lower panel of Fig. 8 give the average values over the two azimuths. It is seen that with increasing Fe coverage the c/a ratio indeed decreases continuously from a value of about 1.33 at 1 ML Fe and approaches the value of 1.0 for undistorted bcc-Fe above 13.5 ML.

For the precise c/a determination by XPD the effect of multiple electron scattering (MS) has to be considered as a correction. By comparing experimental IADs with MS calculations for the fcc-Fe/Ni(0 0 1) system Gazzadi et al. [33] have shown that the polar angular difference between the ideal value of $\theta_{FS} = 35.3°$ for fcc[1 1 2] atomic rows ($c/a = \sqrt{2}$) and the corresponding experimental value of 36.8° for the clean Ni(0 0 1) substrate (which corresponds to c/a value of 1.34 only) is caused by MS effects. On the bcc-Fe side, on the other hand, such an angular difference (or difference in c/a values) was not observed in Ref. [33], in agreement with our results for Fe coverages > 13.5 ML. Therefore, in order to take MS effects into account, our experimental average data points for c/a were corrected by a factor $\sqrt{2}/1.33 = 1.06$ at zero Fe coverage, by a factor of 1.00 at $t = 13.5$ ML Fe and above, and by a linear interpolation between these factors for intermediary Fe thicknesses, $0 < t < 13.5$ ML. These corrected c/a values are shown as filled diamonds in the lower panel of Fig. 8. They show an approximately linear behaviour with a slope of $\Delta(c/a)/\Delta t = 0.034\ (\mathrm{ML})^{-1}$ up to about 11.5 ML, before the value of undistorted bcc-Fe ($c/a = 1.00$) is approached.

3.2.4. Strength of the FS peaks and conclusions for the thickness dependent growth of Fe film

One of the prominent uses of photoelectron spectroscopy is the characterization of the film growth mode. Common types of film growth are: (i) Layer-by-layer, in which the deposited material completes one monolayer, then the second, etc. (FM growth; FM1). (ii) Layer-plus-islanding, in which the first layer completely covers the surface of the substrate and subsequent layer form islands (Stranski–Krastanov growth; SK). (iii) Complete islanding, in which the deposited material immediately forms islands on the surface (Volmer–Weber growth, VW). In addition, the following growth modes are also of interest: (iv) FM growth with an additional (segregated) Au layer (surfactant layer) on top of each Fe layer (FM + Au). (v) Bilayer-by-bilayer FM growth (FM2). (vi) FM growth with complete interdiffusion, in which every second regular film atom site is occupied by a substrate atom (FM + I).

FM + Au growth has been found in our AR-XPS/XPD study of Fe/Au(0 0 1) [32] for Fe film coverages up to 4–6 ML. To demonstrate this growth mode we have compared the experimental data for certain next-neighbour FS enhancements (FSE) in the IADs with the predictions of a simple model for the development of these FSEs with increasing Fe film thickness. The model assumes that the FSE for one emitter is maximum in case of a single scatterer and completely disappears in case of four scatterers. This approximation models

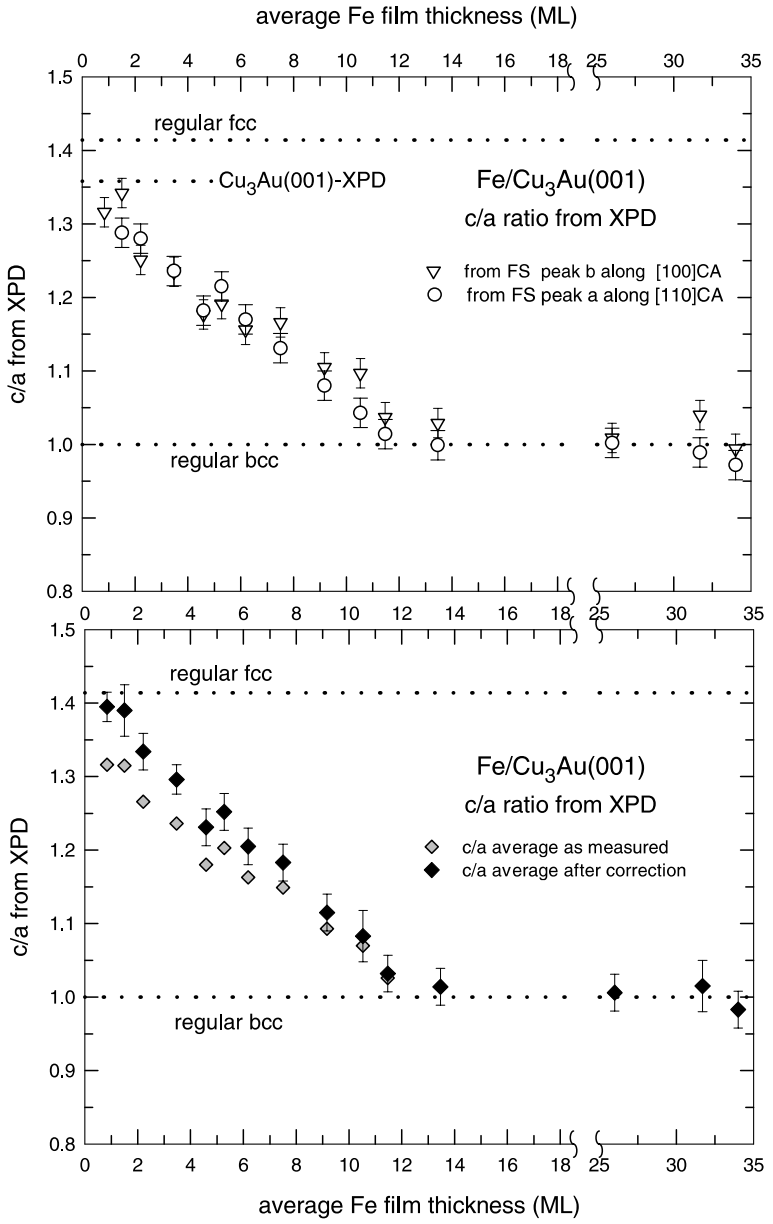

Fig. 8. Above: c/a ratio as calculated from the angular positions FS XPD peaks a and b in the XPD polar anisotropy data given in Fig. 7. The measured value for the clean substrate is labeled by $Cu_3Au(0\,0\,1)$-XPD. Below: Azimuthal average of the two c/a data sets presented above (diamonds with grey colour) and corrected values (black symbols). Error bars are only given for the corrected data. Details of the correction procedure are described in the text. In both panels the dotted lines indicate the c/a values for regular fcc(0 0 1) and bcc(0 0 1) structure, respectively (see Fig. 6), and the measured c/a value from clean $Cu_3Au(0\,0\,1)$.

the combined effect of multiple FS and inelastic scattering. In this model, the different growth modes can be distinguished easily by the onset N_0 (in ML) of the film FSE, its initial slope and the number of layers, where saturation is reached (N_{sat} in ML). For further details and the application of

the model on the different growth modes we refer to Ref. [32].

The most important results for the development of the Fe FSEs with increasing Fe coverage, relevant to the work reported here, are: (a) Both for the fcc and bcc structure (Fig. 6), the first Fe layer (or the surface layer of a multilayer film) produces an isotropic intensity pattern because there are no scatterer in the direction of the detector for any given position of the latter. This is only true if there have no substrate atoms segregated on top of the Fe atoms. (b) Along the surface normal and the direction a in the [1 1 0]CA azimuth in Fig. 6 ([1 0 1]Fe for bcc growth and [1 1 2]Fe for fcc growth, respectively), the onset of FSE occurs with the growth of the third layer (which may also be the second Fe layer in case of a surfactant Au layer on top), because the second layer of the film does not scatter the emission from the first layer on top of the substrate (etc.): $N_0 = 2$ and $N_{sat} = 8$ for FM1 and FM2 growth and $N_0 = 1$ and $N_{sat} = 7$ for FM + Au growth. (c) Along the direction b in the [1 0 0]CA azimuth ([1 1 1]Fe in case of bcc growth and [1 0 1]Fe for fcc growth, respectively), every layer above an Fe emitter contributes to FSE: $N_0 = 1$ and $N_{sat} = 4$ for FM1 growth, $N_0 = 1$ and $N_{sat} = 4$ for FM2, $N_0 = 1$ and $N_{sat} = 3$ for FM + Au.

The experimental FSE (or anisotropy) along an internuclear axis found at polar angle θ_{FS} of the maximum of an FS feature may be defined as:

$$\mathrm{FSE}(\theta_{FS}) := I_{FS}(\theta_{FS}) - \mathrm{ISO}(\theta_{FS}). \quad (6)$$

One may also take the integral intensity of an FS feature above the isotropic emission background (see Fig. 6). Because we could not observe any change of the widths of the FS features with increasing film thickness, the integral measure for the FSE does not yield different data sets (within the experimental errors; also checked by Gaussian fits to the FS peaks). Therefore we took the average values of both measures for the FSE.

The dependence of the Fe3p FSEs of the features n, a and b of Fig. 7 on Fe film thickness is presented in Fig. 9. The data have been normalized to unity at high coverages. They can be understood within the simple FS model as developed in Ref. [32]. In the [1 1 0]CA azimuth, both for normal emission and direction a in Fig. 6 the onset of FSE occurs at 1 ML (at 1.5 ML both features are well developed). This of course also observed for normal emission along the other azimuth. Further, normal emission FSE exhibits a first saturation plateau at about 7 ML. This already is a strong hint for FM + Au growth, which theoretically should follow the thick solid curve in grey colour. The dashed curve models the simple FM growth. The second increase of the FSE of feature n at about 12 ML and the FSE "hole" of feature a between 3 and 12 ML will be discussed below. FM + Au growth is definitively proven by feature b along [1 0 0]CA, which coincides within the experimental error with the corresponding FM1 + Au model curve, with the characteristic onset and first saturation at 0 ML (precisely at 0.2 ML in experiment) and 3 ML, respectively.

3.2.5. Work function (ARUPS)

Fig. 10 shows the development of the work function change $\Delta\Phi$ of Fe/Cu_3Au(0 0 1) with increasing Fe film thickness. The data have been gathered by measuring the width of complete ARUP spectra (taken with $h\nu = 21.2$ eV) extending from the onset of photoemission (corresponding to $E_{kin} = 0$, E_{kin} is the kinetic energy) to the Fermi edge ($E_{kin} = h\nu - \Phi$). In the thickness range $0 \leqslant t \leqslant 3.5$ ML (region I in Fig. 10), $\Delta\Phi$ shows first a steep decrease and than a saturation. This correspond to the initial increase of the in-plane lattice constant a of the Fe film which subsequently ends up in a plateau between about 3 and 5 ML, as observed with RHEED (Fig. 4, closed circles). When a increases once more, $\Delta\Phi$ decreases again too (region II) and reaches its final saturation value at about 12 ML, when bcc(0 0 1) structure of the Fe film (region III) is already well developed. In conclusion, the development of the work function nicely reflects the structural changes of the growing Fe film; specially the increase of the in-plane lattice parameter a in its very surface region as observed with RHEED is in agreement with a decrease of Φ, because in general a more open surface has a lower work function than a less open surface due to a diminished spill-over of the electron surface density.

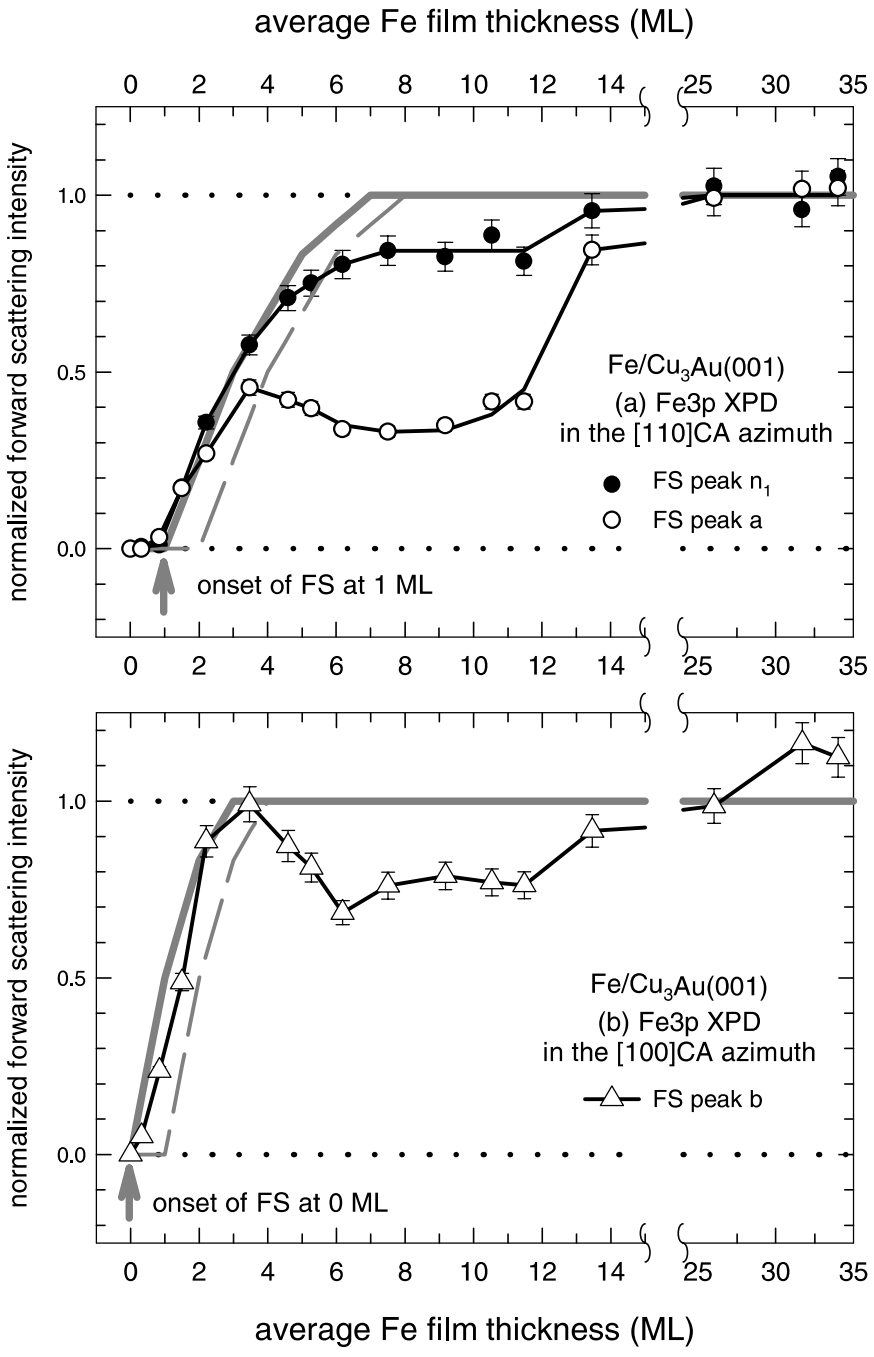

Fig. 9. Strength of the Fe3p FS features (FS enhancement = FSE) as deduced from the data given in Fig. 7 as function of Fe film thickness. Above: Azimuthal average of the FSE of the normal emission FS peaks n_1 and n_2 (●) and FSE of peak a (○) in the emission plane along the [1 1 0]CA substrate azimuth. Below: FSE of peak b in the emission plane along the [1 0 0]CA substrate azimuth. The grey lines give the theoretical dependence of the FSEs according to a model described in the text. The solid line is for layer-by-layer growth with a surfactant Au layer on top (called FM1 + Au in the text), whereas the dashed line is for simple layer-by-layer growth (FM1).

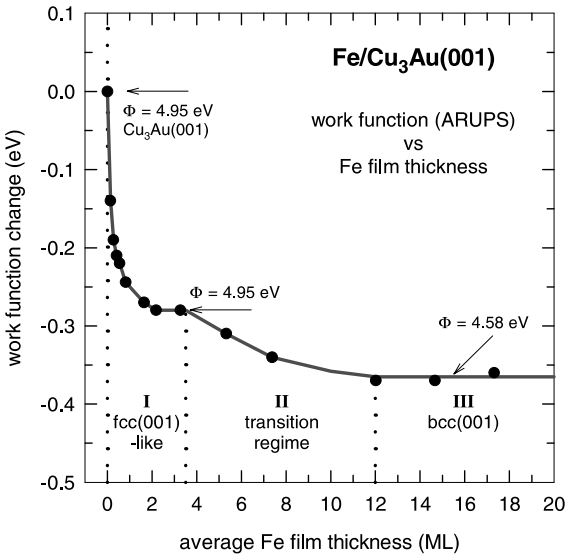

Fig. 10. Change of the work function of Fe/Cu_3Au(0 0 1) with increasing Fe coverage. The data have been measured using ARUPS.

3.2.6. Conclusions from ARXPS and XPD

We conclude that the initial film growth occurs in a multilayer mode (FM + Au) and with an fcc(0 0 1)-like structure. The latter is evident from the occurrence of the fcc-like scattering maxima near 45° and 36° along the [1 0 0]CA and [1 1 0]CA substrate azimuths, respectively, in the early stages of coverage up to about 3.5 ML. At 13.5 ML a well-ordered bcc(0 0 1)-R45° has developed. In the thickness range between ~3.5 and 13.5 ML the fcc-like film is progressively strained along the normal direction by a compression of the interlayer distance, as is evident from the development of the c/a ratio (Section 3.2.3). This compression, however, is accompanied by a movement of the Fe atoms contributing to the FSE out of the detection planes. This is deduced from the FSE "valleys" visible in Fig. 9 and already mentioned above. Because in the XPD experiment the detection planes are fixed (the planes shown in Fig. 6), an out-of-plane movement of the atoms of course results in a decrease of the FSE detectable in these planes. Because the decrease of the FSE effect is very small along the surface normal, the atom movement is approximately described by a rotation about the surface normal, however in an effective sense, meaning that the rotation angle differs from one to the other unit cell. This is in agreement with the results from the RHEED experiment, which could be understood by assuming the presence of twisted crystallographic Fe domains which are rotated about the surface normal.

3.3. Mössbauer spectroscopy

Mössbauer spectroscopy is a unique method in the sense that it provides (via the hyperfine interaction) local (atomistic) information about the magnitude of the Fe atomic moment, the atomic environment and its symmetry around the Fe atom, and about the s-electron density at the ^{57}Fe nucleus in the sample [43]. In a fingerprint-type of way it may give information upon the presence of different magnetic and/or crystallographic phases in the sample.

In situ Mössbauer (CEMS) spectra of 4, 8 and 15 ML Fe on Cu_3Au(0 0 1) at 25 K (i.e. near magnetic saturation) are shown in Fig. 11(a)–(c), respectively. All spectra exhibit Zeeman sextets with large values of the hyperfine magnetic fields or, equivalently, with large Fe atomic moments. All films are magnetically ordered at 25 K. Because of the rather large width of the outer lines, the spectra have been least-squares fit with a distribution of hyperfine fields including a small electric quadrupole interaction. The Mössbauer spectral parameters obtained from the fitting are give in Table 1.

The Mössbauer spectrum of the 15 ML film (Fig. 11(c)) and its parameters (Table 1) are rather close to bulk bcc Fe (for comparison: $B_{hf} \approx 34$ T for bulk bcc Fe at 25 K). This agrees with our RHEED and XPD results, summarized in Fig. 12(a), which show that the lattice parameters a and c of 15 ML Fe are those of bcc Fe. Nevertheless, the somewhat larger apparent linewidth ($\Gamma \sim 0.6$ mm/s) and the small quadrupole interaction ($2\varepsilon \sim -0.02$ mm/s) are an indication of some residual strain and/or defects in the 15 ML film. (For comparison, measured values for bulk bcc Fe are $\Gamma \sim 0.3$ mm/s and $2\varepsilon = 0$ mm/s).

By contrast, the spectrum of 4 ML Fe (Fig. 11(a)) and its spectral parameters (Table 1) are distinctly different from those of the 15 ML bcc-Fe

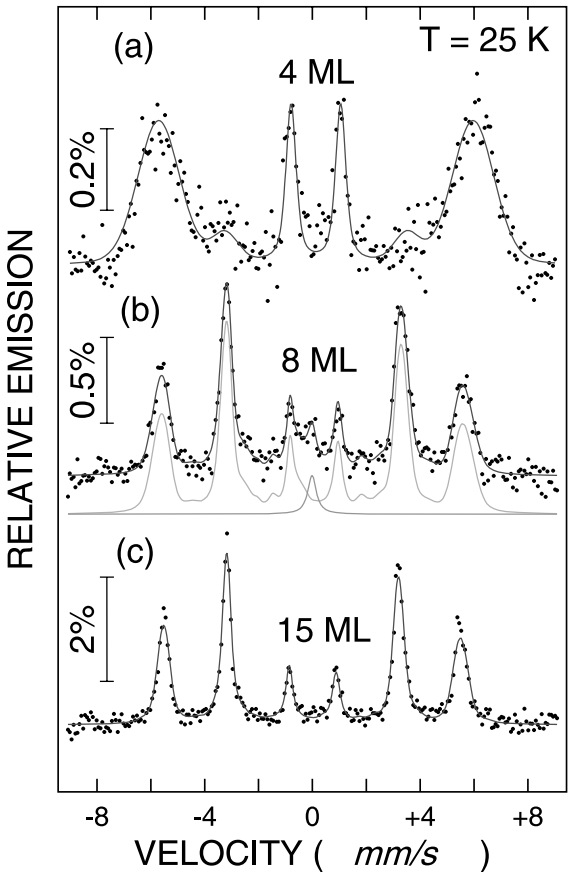

Fig. 11. In situ Mössbauer spectra (CEMS) of Fe/Cu_3Au(0 0 1) in UHV at 25 K for Fe coverages of (a) 4.0 ML (fct-Fe), (b) 8.0 ML (bct-Fe) and (c) 15 ML (bcc Fe). The drawn lines are least-squares fits to the data points.

film (Fig. 11(c)) or from bulk bcc Fe. This agrees with the different crystallographic structures of both films. According to Fig. 12(a) the 4 ML film has the fct structure (compressed fcc), while the 15 ML film is bcc. Thus, the spectrum in Fig. 11(a) is typical for fct Fe. It is characterized by an apparent hyperfine field of ~36 T, a very large apparent line width (1.8 mm/s), and a relatively large (positive) quadrupole interaction of +0.07 mm/s. A similar line broadening for fct 3 ML-Fe/Cu(0 0 1) [11] was ascribed to some kind of structural disorder in the films. This agrees with our present RHEED and XPD results, which are interpreted in terms of a certain degree of structural atomic disorder and/or defects. Moreover, the (noncubic) fct structure of 4 ML Fe is reflected in a measured (positive) quadrupole interaction 2ε, similar to the case of fct 3 ML-Fe/Cu(0 0 1) [11,44].

The 8 ML Fe film has a thickness in the transition region from fct to bcc structure, Fig. 12(a). According to the a and c values in Fig. 12(a), this film has the bct structure (expanded bcc), resulting in the (negative) quadrupole interaction of −0.06 mm/s (Table 1). Its apparent linewidth of 0.9 mm/s is midway between that of 4 and 15 ML Fe. The important feature in Fig. 11 is that the 8 ML spectrum (Fig. 11(b)) is clearly not a superposition of the spectra of fct Fe (Fig. 11(a)) and bcc Fe (Fig. 11(c)). The spectrum of 8 ML Fe and its Mössbauer parameters rather appear as part of a continuous evolution from bcc Fe (Fig. 11(c)) to fct Fe (Fig. 11(a)). Therefore, the coexistence of fct (or fcc) and bct (or bcc) phases in the transition region, i.e. a two-phase structure [17,24], does not exists in our films.

A striking difference in the spectra of Fig. 11 is the drastic reduction of the relative line intensities of lines number 2 and 5 [the ($\Delta m = 0$)-nuclear transitions] for 4 ML Fe (Fig. 11(a) as compared to those of 8 and 15 ML Fe (Fig. 11(b), (c)). (The lines in the Zeeman sextet are labeled no. 1–6 from

Table 1
Mössbauer spectral parameters at 25 K of 4, 8 and 15 ML Fe on Cu_3Au(0 0 1)

	4 ML	8 ML	15 ML
B_{hf} (T)	36.2 ± 0.5	32.4 ± 0.4	33.1 ± 0.3
Γ (mm/s)	1.8 ± 0.1	0.9 ± 0.1	0.6 ± 0.1
ϑ	25.2°	90°	90°
2ε (mm/s)	+0.07 ± 0.02	−0.06 ± 0.01	−0.022 ± 0.007
cs (mm/s)	+0.26 ± 0.08	−0.33 ± 0.09	−0.60 ± 0.08

B_{hf} = average hyperfine magnetic field, Γ = apparent width of outer lines (FWHM), ϑ = average angle between γ-ray direction and Fe spin direction, 2ε = average electric quadrupole interaction, cs = average center line shift relative to bulk bcc-Fe at 300 K.

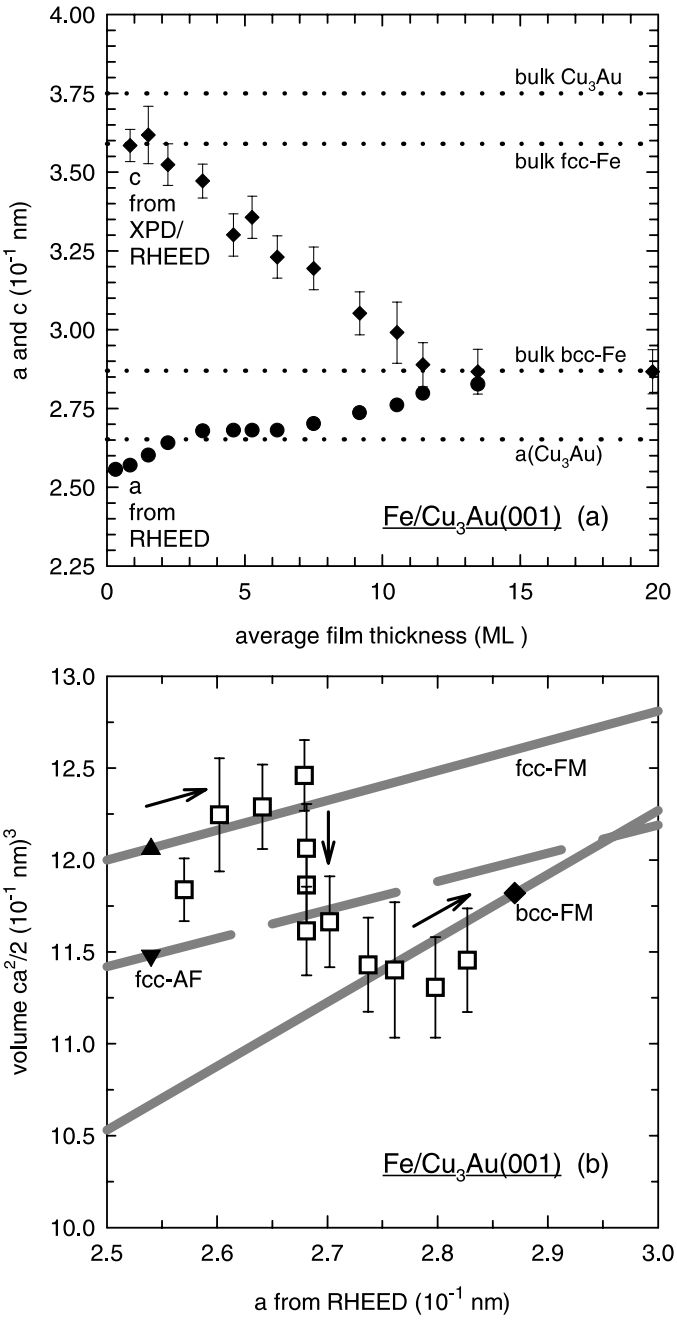

Fig. 12. (a) In-plane lattice parameter a from RHEED and perpendicular lattice parameter c from combining XPD (Fig. 8) and RHEED (Fig. 4) data, as function of Fe film thickness. c is only given for those film thicknesses where XPD measurements have been performed. For the definition of c and a, see Figs. 1 and 5. (b) Fe atomic volume V versus in-plane atomic distance a (□). Also given are volumes V_0 of ferromagnetic high-moment high-volume fct-Fe/Cu(0 0 1) (12.06 Å^3) and of antiferromagnetic low-moment low-volume fcc-Fe/Cu(0 0 1) (11.48 Å^3) according to Refs. [40,46], and V_0 for bulk bcc-Fe (11.8 Å^3). Full straight lines: Theory according to Ref. [18]. The step-like change of V at $a = 2.68$ Å is caused by the change in c at nearly constant a in the film thickness range between about 3.5 and 6.5 ML Fe (see Fig. 4, ●).

left to right). This effect is caused by the different spin orientations (given by the angle ϑ between the incident γ-ray direction or film-normal direction and the direction of B_{hf}, i.e. the spin direction. For the 4 ML film we obtain $\vartheta = 25°$ (Table 1), indicating a strong (but not complete) perpendicular spin orientation (or perpendicular magnetic anisotropy [23–26]). Our result is the direct (atomistic) observation of preferential perpendicular spin orientation in $Fe/Cu_3Au(0\,0\,1)$. The other two samples (8 and 15 ML Fe) exhibit in-plane spin orientation with $\vartheta = 90°$ (Table 1). The change in sign of 2ε is explained by the spin reorientation from nearly perpendicular (at 4 ML) to in-plane orientation (at 8 and 15 ML) [11,44].

The 6.4% enhancement relative to bulk bcc Fe at 25 K of the measured hyperfine field, B_{hf}, in 4 ML Fe can be explained by the additional contribution of the perpendicular demagnetizing field, $B_{dem} \approx \mu_0 M_S \cos\vartheta$, for the case of nearly perpendicular spin orientation [45]. The intrinsic hyperfine field, B_{int}, (which is approximately proportional to the local Fe moment) and B_{dem} both are antiparallel to the perpendicular magnetization direction. (For in-plane magnetization, $B_{dem} = 0$ and $B_{hf} = B_{int}$, as for 8 and 15 ML Fe). For 4 ML Fe we can calculate $B_{int} = B_{hf} - B_{dem} \approx 34.4$ T, taking $\vartheta = 25.2°$ and assuming that fct and bcc Fe have about the same saturation magnetization $\mu_0 M_S$ of about 2 T. Since within error bars the value of 34.4 T is equal to that of bulk bcc Fe and is close to that of 8 and 15 ML Fe (Table 1), we may conclude that the atomic moment of the FM fct high-spin phase is about equal to that of bulk bcc Fe, although the atomic volume of the fct phase is larger (see Fig. 12(b)). There is a small enhancement of about 2.0 ± 0.9 T in the intrinsic hyperfine field, B_{int}, of 4 ML (fct) as compared to 8 ML (bct) Fe which cannot be attributed to the demagnetizing field, but might be related to a small moment enhancement in 4 ML Fe.

The average center line shift at 25 K (cs, relative to bulk bcc-Fe at RT) given in Table 1 includes the chemical shift (isomer shift) and the second-order Doppler (thermal) shift. Assuming thickness-independent Debye temperatures, the changes in cs values with film thickness at 25 K then are variations of the isomer shift. Obviously the isomer shift becomes continuously more positive with decreasing Fe thickness, i.e. in going from the bcc (at 15 ML) to the fct (at 4 ML) structure. This means that the s-electron density at the ^{57}Fe nucleus is continuously reduced in going from the bcc (via the bct) to the fct structure, as expected for a simultaneous increase of the atomic volume, e.g. in the $Fe/Cu(0\,0\,1)$ system [11,44].

In the case of 8 ML Fe, an additional weak single line with a center line shift at 25 K of $+0.091 \pm 0.042$ mm/s (relative to bulk bcc Fe at RT) and $\Gamma = 0.38 \pm 0.14$ mm/s had to be taken into account, contributing 3.8% to the total intensity (spectral area). This single line might be caused by a small fraction of low-moment Fe or, more likely, by a small fraction of rapidly relaxing (superparamagnetic-like) bct Fe islands in the film. We like to mention that the RT Mössbauer spectrum of the 4 ML film was rather smeared out and exhibited extremely broad lines, typical for thermally fluctuating Fe moments with relaxation times of the order of the Mössbauer life time of $\sim 10^{-7}$ s. A single line has been observed earlier in the $Fe/Cu_3Au(0\,0\,1)$ system [20].

4. Atomic volume and epitaxial lines

The combination of our RHEED and XPD results, i.e. the film-thickness dependence of the in-plane atomic distance, a, and the perpendicular lattice parameter, c, is shown in Fig. 12(a). With increasing Fe coverage the c parameter is continuously and about linearly compressed, while simultaneously the a parameter is continuously expanded. This means the observation of a continuous Bain transformation from fcc to bcc structure in our films. We like to emphasize again that there is a thickness region between ~3.5 and 6.5 ML Fe, where the in-plane distance, a, shows plateau-like behavior and remains nearly constant at ~2.68 Å, which is close to the in-plane atomic distance (2.652 Å) of the $Cu_3Au(0\,0\,1)$ substrate. In this region the in-plane lattice parameter of the growing film appears to be clamped by epitaxial interaction with the substrate surface.

Epitaxy produces large strains in the overlayer, in our case tensile in-plane strain and compressive

out-of-plane strain, leading to tetragonal states with different atomic volumes. Marcus and Jona [18] have calculated "epitaxial lines" for the tetragonal structural strained fcc and bcc Fe under the assumption that the Poisson ratios and elastic moduli of fcc and bcc Fe films remain constant during the deformation, and that they can be described by bulk elastic constants. The epitaxial line that relates the Fe atomic volume, $V = ca^2/2$, of a tetragonal state to its in-plane atomic spacing, a, is obtained by integration of Eq. (6) in Ref. [18] as:

$$V = V_0(a/a_0)^{2-\gamma} \tag{7}$$

where $\gamma = 2v/(1-v)$ and the Poisson ratio $v = c_{12}/(c_{11}+c_{12})$, with elastic constants c_{11} and c_{12}. V_0 is the atomic volume of the unstrained, equilibrium film structure (fcc or bcc in our case). In Fig. 12(b) the epitaxial line for the different states of iron are shown. For the calculation a value $\gamma_{fcc} = 1.64$ and $\gamma_{bcc} = 1.16$ was used [26], and $V_0 = 11.8$ Å^3 was taken for bcc Fe. Fcc Fe appears in two different equilibrium states which are epitaxially stabilized in the Fe/Cu(0 0 1) system: a ferromagnetic (FM) high-volume state with $V_0 =$ 12.06 Å^3, and an antiferromagnetic (AF) low-volume state with $V_0 = 11.48$ Å^3 (both values according to Ref. [46] and corrected for in-plane spacing in Ref. [40]). Our experimental V values, obtained from the data in Fig. 12(a), are also shown in Fig. 12(b) (open squares). For small Fe thicknesses ($t \lesssim 3.5$ ML) and $a \lesssim 2.68$ Å, the experimental data are closest to the epitaxial line of FM high-volume fcc Fe (fcc-FM), and, consequently, the structure of these films is fct. For the thickest films in the region $9 \lesssim t \lesssim 13.5$ ML and $a \gtrsim 2.74$ Å our experimental values are closest to the epitaxial line of bcc Fe (bcc-Fe); therefore, their structure is bct, in agreement with results by Schirmer et al. [26]. For the medium thickness region $3.5 \lesssim t \lesssim 7.5$ ML, which contains the plateau in the a values at 2.68 Å (Fig. 12(a)), a step-like drop from fct states to bct states is observed by increasing the film thickness. This crossover between tetragonal states seems to resemble a first-order phase transition. Indeed, Krasko and Olson [2] have calculated the ground-state enthalpy curve along the Bain deformation path of iron and predicted a first-order phase transition between FM bcc-like states and fcc-like states (the latter being non-magnetic, however, and not FM like in our case), accompanied by a volume discontinuity at a critical ratio $c/a = 1.23$. According to Fig. 8 (bottom panel) this critical ratio corresponds to a film thickness of 6 ML Fe with an in-plane atomic distance of 2.68 Å, which is the a value, where we indeed observe the volume discontinuity in Fig.12(b). However, we do not think that the latter is related to a first-order transition, since the c-parameter behaves continuously in that region (Fig. 12(a)), with the a values remaining about constant. Moreover, we have not observed a fct and bct two-phase mixture, such as would appear in a nucleation and growth process of a first-order (martensitic) transition.

Therefore, the results (Fig. 12(a)) demonstrate that a continuous Bain transformation takes place in Fe/Cu_3Au(0 0 1), contrary to the Fe/Cu(0 0 1) system, where a MT was observed [5–8]. According to Fig. 12(b) and to our Mössbauer results (Section 3.3) this transition takes place from ferromagnetic high-moment high-volume fct Fe to ferromagnetic bcc Fe, whereby the atomic volume decreases. By contrast, the usual MT involves a transition from a non-magnetic fcc to a FM bct (or bcc) state, whereby the atomic volume increases [1,4]. It is the magneto-volume effect in fct Fe that causes this different behavior.

5. Summary

The structure of epitaxial Fe films on Cu_3Au(0 0 1) was precisely determined by RHEED and XPD. With increasing film thickness a nearly linear continuous compression of the perpendicular lattice parameter, c, and a simultaneous continuous expansion of the in-plane atomic distance, a, was observed. Films with thicknesses between ~1 and 12 ML do not grow pseudomorphous, but appear to form twisted crystallographic domains including some kind of atomic disorder. Apparently, the strain energy induced by the compressed perpendicular interlayer spacing is lowered by rotating the planar Fe unit mesh array from the surface mesh of the substrate. Films thinner than

~2 ML are fct and show reduced in-plane spacings as compared to the substrate surface due to island growth and lattice relaxation. Up to ~3.5 ML the film structure is fct. There is an intermediate region between ~3.5 and 6.5 ML, where the in-plane atomic spacing of ~2.68 Å remains nearly independent of thickness, while the perpendicular spacing c changes continuously. Above 6.5 ML thickness the films have bct structure, and a as well as c approach bulk bcc-Fe values at ~13.5 ML. The observed continuous compression of c and the simultaneous continuous expansion of a implies that a continuous fcc–bcc Bain transformation takes place in the Fe/Cu_3Au(0 0 1) system with increasing film thickness, contrary to the Fe/Cu(0 0 1) system, where a discontinuous MT is known to exist. We speculate that Au atoms observed to be present at the Fe film surface in the case of Fe/Cu_3Au(0 0 1) act as surfactants and prevent the MT. The atomic volume of the tetragonal states was found to be close to fct or bct epitaxial lines [18]. A crossover from ferromagnetic high-moment high-volume fct to bct Fe was found to occur in the intermediate thickness range between ~3.5 and 6.5 ML where a is nearly constant. CEMS was used to prove that a fct-plus-bct two-phase structure does not exist. Fct films are in a high-moment FM state. The Mössbauer results also prove that the structural changes observed by RHEED and XPD (which are surface sensitive techniques) do not occur only in the surface region, but seize the film as a whole.

Correlated with the Bain transformation is a spin reorientation from preferentially perpendicular (for fct structure) to in-plane (for bct structure) spin direction at 25 K.

Acknowledgements

We thank U. von Hörsten for his expert technical assistance. We are also grateful to Dr. H. Bach (Bochum) for growing and providing the Cu_3Au single crystals. This work was supported by the Deutsche Forschungsgemeinschaft (SFB 491, SFB 166) and Graduirtenkolleg "Struktur und Dynamik heterogener Systeme".

References

[1] Z. Nishiyama, Martensitic Transformations, Academic, New York, 1978.
[2] G.L. Krasko, G.B. Olson, Phys. Rev. B 40 (1989) 11536, and references therein.
[3] H.C. Herper, E. Hoffmann, P. Entel, J. Physique IV France 7 (1997) C5–71.
[4] E.F. Wassermann, M. Acet, P. Entel, W. Pepperhoff, J. Magn. Soc. Jpn. 23 (1999) 385.
[5] K. Kalki, D.D. Chambliss, K.E. Johnson, R.J. Wilson, S. Chiang, Phys. Rev. B 48 (1993) 18344.
[6] M. Wuttig, B. Feldmann, J. Thomassen, F. May, H. Zillger, A. Brodde, H. Hannemann, H. Neddermeyer, Surf. Sci. 291 (1993) 14.
[7] J. Giergiel, J. Kirschner, J. Landgraf, J. Shen, J. Woltersdorf, Surf. Sci. 310 (1994) 1.
[8] A. Kirilyuk, J. Giergiel, J. Shen, M. Straub, J. Kirschner, Phys. Rev. B 54 (1996) 1050.
[9] N. Memmel, Th. Detzel, Surf. Sci. 307 (1994) 490.
[10] P. Schmailzl, K. Schmidt, P. Bayer, R. Doell, K. Heinz, Surf. Sci. 312 (1994) 73.
[11] W. Keune, A. Schatz, R.D. Ellerbrock, A. Fuest, K. Wilmers, R.A. Brand, J. Appl. Phys. 79 (1996) 4265.
[12] K. Kadau, R. Meyer, P. Entel, Surf. Rev. Lett. 6 (1990) 35.
[13] E.C. Bain, Trans. AIME 70 (1924) 25.
[14] P. Alippi, P.M. Marcus, M. Scheffler, Phys. Rev. Lett. 78 (1997) 3892.
[15] M.G. Donato, P. Ballone, P.V. Giaquinta, Phys. Rev. B 61 (2000) 24.
[16] E. Hahn, E. Kampshoff, N. Wälchli, K. Kern, Phys. Rev. Lett. 74 (1995) 1803.
[17] M.-T. Lin, J. Shen, W. Kuch, H. Jenniches, M. Klaua, C.M. Schneider, J. Kirschner, Surf. Sci. 410 (1998) 290.
[18] P.M. Marcus, F. Jona, Surf. Rev. Lett. 1 (1994) 15.
[19] S.H. Lu, J. Quinn, D. Tian, F. Jona, P.M. Marcus, Surf. Sci. 209 (1989) 364.
[20] W.A.A. Macedo, W. Keune, R.D. Ellerbrock, J. Magn. Magn. Mater. 93 (1991) 552.
[21] R. Rochow, C. Carbone, Th. Dodt, F.P. Johnen, E. Kisker, Phys. Rev. B 41 (1990) 3426.
[22] D. Tillmann, E. Kisker, Solid State Commun. 100 (1996) 415.
[23] F. Baudelet, M.-T. Lin, W. Kuch, K. Meinel, B. Choi, C.M. Schneider, J. Kirschner, Phys. Rev. B 51 (1995) 12563.
[24] M.-T. Lin, J. Shen, W. Kuch, H. Jenniches, M. Klaua, C.M. Schneider, J. Kirschner, Phys. Rev. B 55 (1997) 5886.
[25] B. Feldmann, B. Schirmer, A. Sokoll, M. Wuttig, Phys. Rev. B 57 (1998) 1014.
[26] B. Schirmer, B. Feldmann, M. Wuttig, Phys. Rev. B 58 (1998) 4984.
[27] V.I. Moruzzi, P.M. Marcus, J. Kübler, Phys. Rev. B 39 (1989) 6957, and references cited therein.
[28] C.H. Herper, E. Hoffmann, P. Entel, Phys. Rev. B 60 (1999) 3839, and references cited therein.

[29] T. Shinjo, W. Keune, J. Magn. Magn. Mater. 200 (1999) 598, and references therein.
[30] C.S. Fadley, in: R.Z. Bachrach (Ed.), Synchrotron Radiation Research: Advances in Surface and Interface Science, Plenum, New York, 1992.
[31] W.J. Egelhoff Jr., in: J.A.C. Bland, B. Heinrich (Eds.), Ultrathin Magnetic Structures, Springer, Berlin, 1994.
[32] R. Opitz, S. Löbus, A. Thissen, R. Courths, Surf. Sci. 370 (1997) 293.
[33] G.C. Gazzadi, P. Luches, A. di Bona, L. Marassi, L. Pasquali, S. Valeri, S. Nannarone, Phys. Rev. B 61 (2000) 2246.
[34] B. Roldan Cuenya, M. Doi, T. Ruckert, W. Keune, T. Steffl, J. Phys. Soc. Jpn. 69 (Suppl. A) (2000) 125.
[35] W. Kiauka, C. van Cuyck, W. Keune, Mater. Sci. Eng. B 12 (1992) 273.
[36] S. Löbus, M. Lau, R. Courths, S. Halilov, Surf. Sci. 287/288 (1993) 568.
[37] S. Löbus, R. Courths, S. Halilov, H. Gollisch, R. Feder, Surf. Rev. Lett. 3 (1996) 1749.
[38] R. Courths, S. Löbus, S. Halilov, T. Scheunemann, H. Gollisch, R. Feder, Phys. Rev. B 60 (1999) 8055.
[39] J. Fassbender, U. May, B. Schirmer, R.M. Jungblut, B. Hillebrands, G. Güntherodt, Phys. Rev. Lett. 75 (1995) 4476.
[40] A. Schatz, W. Keune, Surf. Sci. 440 (1999) L841.
[41] R.W. Balluffi, Y. Komem, T. Schober, Surf. Sci. 31 (1972) 68.
[42] M.P. Seah, W.A. Dench, Surf. Interf. Anal. 1 (1978) 2.
[43] G.K. Wertheim, Mössbauer Effect: Principles and Applications, Academic, New York, 1964.
[44] R.D. Ellerbrock, A. Fuest, A. Schatz, W. Keune, R.A. Brand, Phys. Rev. Lett. 74 (1995) 3053.
[45] B. Scholz, R.A. Brand, W. Keune, Phys. Rev. B 50 (1994) 2537.
[46] S. Müller, P. Bayer, C. Reischl, K. Heinz, B. Feldmann, H. Zillgen, M. Wuttig, Phys. Rev. Lett 74 (1995) 765.